JOURNAL OF AIRCRAFT
Vol. 36, No. 6, November–December 1999

Structural Optimization of Flight Vehicles with Computational-Fluid-Dynamics–Based Maneuver Loads

Daniella E. Raveh* and Mordechay Karpel†
Technion—Israel Institute of Technology, Haifa 32000, Israel

A methodology of performing structural optimization with static aeroelastic considerations is presented for which the aerodynamic loads are provided by nonlinear computational aerodynamics schemes. Two main subjects that are studied are the evaluation of airloads on a maneuvering flexible aircraft and their integration with a structural optimization code. A computational aerodynamics code originally developed for solving Euler or Navier–Stokes equations for a fixed-shape configuration is modified to incorporate aeroelastic effects. Computational efficiency is obtained when several aeroelastic trim corrections and optimization runs are performed during the process of flowfield convergence, such that the aerodynamic loads and the structural design converge simultaneously. A modal structural model is used for elastic-shape updates, and a trim corrections algorithm is used for varying the incidences and control surface deflections for obtaining user-defined maneuvers. The nonlinear maneuver loads can be combined with linear design cases in a multidisciplinary structural optimization scheme. The method is demonstrated with a wing–fuselage–elevator transport aircraft model performing symmetric and antisymmetric maneuvers at Mach 0.85. The number of iterations required for convergence of the combined maneuver–optimization analysis is typically almost the same as that of regular computational aerodynamics analysis for a fixed-shape configuration.

Introduction

IN the design process of an aircraft structure, after the basic aerodynamic shape and the structural layout are defined, structural optimization is carried out to determine the values of the structural design variables that satisfy the design constraints with minimal weight. The design optimization typically accounts for constraints from several disciplines, including structural stresses and displacements, aeroelastic load distribution and control effectiveness, flutter, gust response, and others. Commercial structural optimization systems such as Automated Structural Optimization System (ASTROS)[1] and MSC/NASTRAN[2] evaluate the aerodynamic forces by use of linear aerodynamic panel methods, such as Unified Subsonic and Supersonic Aerodynamic Analysis (USSAERO)[3] and the doublet-lattice method[4] (DLM), in which the flow equations are formulated based on the linearized aerodynamic potential equations. Although these methods provide rapid and adequately accurate estimations of the aerodynamic loads in the subsonic speed range, they might be inadequate when used for the transonic speed range, in which embedded shock waves affect the flowfield significantly. A better evaluation of the aerodynamic loads can be obtained from higher approximations such as the nonlinear potential model, the Euler equations for inviscid flows, and the Navier–Stokes equations for viscous flows.

The nonlinear aerodynamic solvers belong to the area of computational fluid dynamics (CFD). Most CFD routines for solving the Euler/Navier–Stokes equations for realistic aircraft configurations are developed for dealing with a given fixed aerodynamic shape and typically require large computational resources. CFD analyses are not yet used in structural optimization tasks for the following reasons: 1) They do not have a mechanism for varying the angle of attack and control surface deflections required for trimming the aircraft in prescribed maneuvers, and also do not have a mechanism for changing the shape because of aeroelastic effects; 2) a high computational cost is associated with repeated CFD analyses.

Presented as Paper 98-4832 at the AIAA/USAF/NASA/ISSMO Symposium on Multidisciplinary Analysis and Optimization, St. Louis, MO, 2–4 September 1998; received 10 November 1998; revision received 23 February 1999; accepted for publication 23 February 1999.

*Graduate Student, Faculty of Aerospace Engineering. Student Member AIAA.

†Professor, Faculty of Aerospace Engineering. Senior Member AIAA.

Computational aeroelasticity deals with the integration of CFD schemes with structural models for the computation of the aerodynamic loading on elastic flight vehicles, and for the computation of the aerodynamic maneuver loads. The early works that combined CFD with elasticity used simple structural models and were applied to wing models only.[5–7] Tatum and Giles[8] addressed a complete aircraft configuration by using a full potential aerodynamic method, together with an equivalent-plate structural model. They implemented an iterative solution procedure for obtaining aerodynamic loads and structural deformations for the free-flying aircraft at user-specified flight conditions. The model selected by Tatum and Giles was that of a fighter aircraft consisting of only one aerodynamic grid segment. This choice of model was made to meet the requirements of the CFD code used by the authors, which allowed only single-body analysis. Consequently, the aircraft was trimmed only by vectoring the thrust of the engine, and the common combination of varying the incidences and the control surface angles for achieving trim was not studied. Vinh et al.[9] added a trim routine to the Computational Aeroelasticity Program-Transonic Small Disturbance[10] (CAP-TSD) code. Their work suggested a feedback algorithm to obtain vehicle trim during steady-state flowfield convergence. Since the code used is time accurate, stability and control derivatives could also have been estimated from the transient response.

Schuster et al.[11] addressed the problem of computing the flowfield about flexible fighter aircraft operating at extreme flight conditions, such as high angles of attack and high transonic Mach numbers. Since these flows involve strong shock waves and detached boundary layers for which the small disturbance assumption is no longer valid, they based their work on the Lockheed Euler/Navier–Stokes three-dimensional (ENS3D) aerodynamic method combined with an influence-coefficient structural model. A later work of Schuster[12] demonstrated the use of the preceding aeroelastic analysis method for improving the performance of fighter wings through simultaneous application of control surface deflection and aeroelastic twist. Guruswamy[13] performed aeroelastic computations on a wing–fuselage configuration by using an Euler/Navier–Stokes aerodynamic (ENSAERO) method coupled with a finite element beam-type structural model. In a later work, Obayashi and Guruswamy[14] suggested solving the dynamic equations of the structure, instead of the static equations, with added artificial damping to achieve a smooth structural response and therefore prevent instabilities in the fluid dynamics computations.

Karpel et al.[15] introduced an efficient computational scheme for the evaluation of aerodynamic maneuver loads on flexible rockets in supersonic flight, based on an Euler solver. The modal static-aeroelastic approach of Refs. 16 and 17, which was originally developed for linear aerodynamics and exhibited excellent efficiency and accuracy, was used to evaluate the elastic deformations and to trim the free vehicle. Computational efficiency was obtained when a relatively small number of occasional shape deformations and trim updates were applied during flowfield convergence. This scheme was expanded by Raveh et al.[18] to deal, in a practical way, with realistic aircraft whose trimmed condition is achieved through the use of varied incidences, control surface deflections, and rotation rates.

The computational approach of Ref. 18 is broadened in the current study to facilitate the usage of CFD-based maneuver loads in structural optimization. The study focuses on the efficient integration of the maneuver load computations in the structural optimization scheme, in which the main difficulty arises from the facts that the CFD maneuver load analysis is computationally intensive and that repeated analyses are required during the structural optimization. This difficulty is overcome by performing several structural optimizations during the process of CFD flowfield convergence, in which every optimization is done based on the nonconverged aerodynamic maneuver loads. The method is demonstrated with a wing–fuselage–elevator transport aircraft model performing symmetric and antisymmetric maneuvers at Mach 0.85.

Maneuver Load Computations

Aeroelastic deformations and trim corrections were introduced to the Euler version computational code of Yaniv.[19] A semidiscrete finite-volume method that uses central differencing in space with an explicit multistage time-stepping scheme is used in this code. A steady-state solution to the time-dependent Euler equations is obtained by iterating in time using local time steps and implicit residual smoothing. The code was modified to accommodate the aero–structure interaction and the structural optimization discussed below.

Maneuver load analysis for a given structure is performed in three iterative levels. The innermost level contains the original CFD analysis for a fixed configuration that, if iterated until convergence, provides the aerodynamic load distribution on the rigid aircraft with prescribed aerodynamic incidences. The next iterative level introduces the structural elasticity that is combined with the aerodynamic loading to obtain the corresponding deformed shape. This level, if iterated until convergence, provides a load distribution that agrees with the shape distribution of the elastic aircraft. The outermost level contains the maneuver trim loop at which the incidences and the control surface deflection angles are varied to obtain the total aerodynamic forces and moments implied by the user-defined maneuver. As shown in Ref. 18 and demonstrated below in the numerical example, the three iteration levels are combined such that elastic deformations and trim corrections are introduced during the CFD solution convergence. The main advantages of the integrated aeroelastic computation scheme are that typical convergence rates and computational costs are very similar to those of a fixed-shape CFD run.

The use of CFD-based aeroelastic maneuver loads in aircraft structural optimization required the development of a fully automated, efficient, generic aero–structure interaction scheme with minimal data transfer between the two disciplines. The scheme uses the modal approach, which assumes that the structural deformations can be adequately expressed as a linear combination of a set of low-frequency natural vibration modes. Key issues of the interaction scheme are discussed in the following subsections.

Aerodynamic Grid Changes

To account for aeroelastic effects on the aerodynamic computations, the elastic deflections of the structural finite element nodes should be mapped to the aerodynamic grid points. The deflections are mapped first to the structure–aero interface points and then to the entire aerodynamic grid. When the modal approach is taken, the structure–aero interfacing task reduces to mapping the structural vibration modes to the aerodynamic surface grid points before the CFD run starts. Elastic deformations can then be accounted for within the fluid dynamics computations, as shown below, without returning to the structural model.

In the CFD mesh of the numerical example of this work, all of the physical interface surfaces lie on constant $j = 1$ grid surfaces. A most general interpolation scheme would relate the x–y–z displacements of each aerodynamic grid point $(i, 1, k)$ lying on the interface to the structural displacements. The displacement components of an aerodynamic surface grid point would be in this case

$$\{\boldsymbol{u}_A(i,1,k)\} = [\bar{\boldsymbol{T}}_{AS}(x(i,1,k), y(i,1,k), z(i,1,k))]\{\boldsymbol{u}_S\}$$
$$i = 1, \ldots, il, k = 1, \ldots, kl \quad (1)$$

where $[\bar{\boldsymbol{T}}_{AS}]$ is a function of the spatial x–y–z location of the aerodynamic point $(i, 1, k)$ and the vector $\{\boldsymbol{u}_S\}$ includes three displacements, in the x, y, and z directions, for each structural grid point.

To avoid the difficulties in the application of such three-dimensional interpolation methods, some practical constraining rules are applied, pertinent to interface matters only. It is assumed that the aircraft components can be divided into lifting surfaces and slender bodies and that each lifting surface can be divided into subsurfaces, as described in the next paragraph. Following this division, the interface is performed in two steps: the first step involves mapping of the displacements for each component separately and the second step involves matching of displacements at the components boundaries.

For the mapping of displacements to lifting surfaces, an assumption is made that each lifting surface can be represented by one or more planar reference surfaces, in which the displacements are limited to a direction perpendicular to the plane. Under this assumption, with a reference plane defined by a local ξ–η coordinate system, the displacements $\boldsymbol{u}_A(i, 1, k)$ of an aerodynamic point $(i, 1, k)$ perpendicular to the reference plane are

$$\boldsymbol{u}_A(i,1,k) = [\bar{\boldsymbol{T}}_{AS}(\xi(i,1,k), \eta(i,1,k))]\{\boldsymbol{u}_S\}$$
$$i = 1, \ldots, il, k = 1, \ldots, kl \quad (2)$$

where $\bar{\boldsymbol{T}}_{AS}$ is a row transformation vector that is a function of ξ and η only and $\{\boldsymbol{u}_S\}$ is the vector of structural displacement in which every element represents the displacement of one structural point in the direction perpendicular to the reference plane. Displacement mapping is performed for each reference plane separately; the infinite plate spline (IPS) method by Harder and Desmarais[20] is applied, which compares the spline surface with an infinite plate that bends in reaction to a set of loads such that it obtains the known displacements at the structural spline points.

For mapping of displacements to slender bodies, an assumption is made that each slender body can be represented by a reference beam capable of lateral bending and possibly torsion. Under this assumption, with a reference beam defined by a local ξ coordinate, the displacements $\boldsymbol{u}_A(i, 1, k)$ of an aerodynamic point $(i, 1, k)$ perpendicular to the reference beam are

$$\boldsymbol{u}_A(i,1,k) = [\bar{\boldsymbol{T}}_{AS}(\xi(i,1,k))]\{\boldsymbol{u}_S\}$$
$$i = 1, \ldots, il, k = 1, \ldots, kl \quad (3)$$

where $\bar{\boldsymbol{T}}_{AS}$ is a row transformation vector that is a function of ξ only and $\{\boldsymbol{u}_S\}$ is a vector containing structural displacements and twists. Displacement mapping for each slender beam is obtained by application of the beam spline method.[21] Following the same logic of the IPS method, the beam spline method compares the bending slender body with a beam that bends in reaction to a set of lateral loads such that it obtains the known displacements and twists at the structural spline points.

At the end of this first step of the mapping, the reference plane or the reference beam of each segment has its own transformation matrix:

$$\{\boldsymbol{u}_A\}_{\text{seg}} = [\boldsymbol{T}_{AS}]_{\text{seg}}\{\boldsymbol{u}_S\}_{\text{seg}} \quad (4)$$

where $[\boldsymbol{T}_{AS}]_{\text{seg}}$ is the assembly of the row transformation vectors $[\bar{\boldsymbol{T}}_{AS}]$ in Eq. (2) for a reference plane or in Eq. (3) for a reference beam.

The second step of the mapping involves matching of the boundary displacements between segments that have different splines. A displacement matching algorithm, based on a tree hierarchy, is applied, in which the fuselage serves as the trunk and the components coming out of it serve as the branches. Each branch can serve as a trunk to lower hierarchy components. The deformation of a branch point is determined by the branch's own spline, Eq. (4), plus a correcting displacement that maintains the branch interface with the trunk. A correcting displacement is applied uniformly to all the points along each i-constant grid line of the branch component. The value of the correcting displacement is determined such that the first point of the grid line is attached to the trunk.

The structure–aero displacement mapping is applied to the elastic-mode matrix $[\phi]$ to yield the modal displacements in the aerodynamic grid $[\phi_A]$. Mapping the mode shapes in the current study was done by dividing the aircraft into fuselage, wing, and elevator components, applying the beam spline method to displacement mapping at the fuselage, and applying the IPS method to displacement mapping of the wing and the elevator. The wing and the elevator were each represented by one reference plane.

The elastic-shape deformations of the aerodynamic surface grids are obtained, according to the modal approach to static aeroelasticity,[16] as a linear sum of a set of mode shapes $[\phi_A]$:

$$\{\boldsymbol{u}_{AE}\} = [\phi_A]\{\boldsymbol{\xi}_E\} \tag{5}$$

where $\{\boldsymbol{\xi}_E\}$ is the generalized elastic displacement vector.

Once the aerodynamic grid points that lie on the interface surfaces have been deflected to account for the structural deformations, the field grids must also be deflected accordingly. The deformed grid should satisfy a few basic requirements: Grid lines of the same family should not intersect, the updated grid should remain fairly smooth, and the grid deformations should decay rapidly such that points near the deformed surface move with the surface whereas points near the far field do not move significantly.

The grid is regenerated in two steps: First, the $j = 1$ surfaces ahead, behind, and beside the interface surfaces are adjusted so that they meet the displaced boundaries of the interface surfaces. Then the remaining grid points are redistributed, following the way suggested by Schuster et al.,[11] in which each grid point along an η grid line is moved in the same direction as the $j = 1$ point by distance

$$\Delta_j = \Delta Y_1[1 - (S_j/S_{\text{gl}})] \tag{6}$$

where S_j is the arc length between the j grid point and the last grid point on a grid line, and S_{gl} is the arc length of a grid line.

Structural Elastic Deformations

The static equilibrium equation in generalized coordinates is

$$[K_E]\{\boldsymbol{\xi}_E\} = \{\boldsymbol{F}_E\} \tag{7}$$

where $[K_E]$ is the generalized stiffness matrix associated with $[\phi_E]$ and $\{\boldsymbol{F}_E\}$ is the associated generalized aerodynamic force vector. The generalized forces are obtained by

$$\{\boldsymbol{F}_E\} = [\phi_A]^T(\{\boldsymbol{F}_A\} - \{\boldsymbol{F}_C\}) \tag{8}$$

where $\{\boldsymbol{F}_A\}$ is the aerodynamic force vector at the aerodynamic surface grid points, defined by the local pressure, area, and surface orientation. The reference aerodynamic shape can be defined either by the jig shape, that is, the unstressed shape, and then $\{\boldsymbol{F}_C\} = 0$, or by the cruise shape, and then $\{\boldsymbol{F}_C\}$ is a vector of loads associated with the shape at nominal cruise conditions, defined in a previous aerodynamic analysis.

Orthogonality of the rigid-body and the elastic modes with respect to the structural mass and stiffness matrices implies that $[K_E]$ is diagonal and that inertia relief effects on the right-hand side of Eq. (7) are taken care of automatically.[16] The rigid-body counterpart of Eq. (7) is used below in the maneuver trim process.

When the modal approach is used, the modal stiffness matrix and the mode matrix are the only structural data required for the maneuver load analysis. These matrices are calculated by the finite element code and are read in the CFD run as it starts and after each structural optimization run. Because the number of structural modes used is typically small (in this work 15 structural modes were found to be conservatively sufficient), very little structural data are required to be transferred.

Maneuver Trim

Most structural design cases are based on aerodynamic loads of prescribed aircraft steady maneuvers defined by the rigid-body accelerations $\{\ddot{\boldsymbol{\xi}}_R\}$. The required aerodynamic lift and moment coefficients, C_L and C_M, respectively, in symmetric maneuvers are related to $\{\ddot{\boldsymbol{\xi}}_R\}$ by

$$qS\begin{Bmatrix} C_L \\ C_M\bar{c} \end{Bmatrix}_{\text{req}} = [M_R]\{\ddot{\boldsymbol{\xi}}_R\} \tag{9}$$

where $\bar{c}$ is the reference chord, S is the reference area, and q is the dynamic pressure. The mass matrix $[M_R]$ is associated with the rigid-body mode matrix $[\phi_R]$ in which the first mode reflects a unit heave and the second reflects a unit pitch about the center of gravity. Similar expressions can be written for antisymmetric or asymmetric maneuvers.

The CFD run starts with an initial estimate of the trim variables, which are updated during the flowfield convergence according to the differences between the required and the current values of the aerodynamic coefficients. The current values are calculated during the CFD solution by

$$\begin{Bmatrix} C_L \\ C_M\bar{c} \end{Bmatrix}_{\text{cur}} = \frac{1}{qS}[\phi_R]^T\{\boldsymbol{F}_A\} \tag{10}$$

The angle of attack α and elevator deflection δ are corrected in a symmetric maneuver by

$$\begin{Bmatrix} \alpha \\ \delta \end{Bmatrix}_{\text{new}} = \begin{Bmatrix} \alpha \\ \delta \end{Bmatrix} + \begin{Bmatrix} \Delta\alpha \\ \Delta\delta \end{Bmatrix} \tag{11}$$

where

$$\begin{Bmatrix} \Delta\alpha \\ \Delta\delta \end{Bmatrix} = \begin{bmatrix} \tilde{C}_{L\alpha} & \tilde{C}_{L\delta} \\ \tilde{C}_{M\alpha}\bar{c} & \tilde{C}_{M\delta}\bar{c} \end{bmatrix}^{-1}\left(\begin{Bmatrix} C_L \\ C_M\bar{c} \end{Bmatrix}_{\text{req}} - \begin{Bmatrix} C_L \\ C_M\bar{c} \end{Bmatrix}_{\text{cur}}\right) \tag{12}$$

where $\tilde{C}_{L\alpha}$, $\tilde{C}_{M\alpha}$, $\tilde{C}_{L\delta}$, and $\tilde{C}_{M\delta}$ are the estimated derivatives of the aerodynamic coefficients with respect to the symmetric trim variables. With nonlinear CFD analysis, these values are not available explicitly. They can be obtained from a computationally expensive finite-difference analysis, but this is not necessary because trim convergence is likely to occur even with rough estimates of the derivatives, such as the linear aerodynamic derivatives, as demonstrated by the numerical example. Earlier studies[18] showed that in cases for which the coupling between the angle of attack and the elevator is weak, i.e., the angle of attack mainly controls the lift coefficient and the elevator deflection angle mainly controls the moment coefficient, the coupling terms $\tilde{C}_{M\alpha}$, $\tilde{C}_{L\delta}$ can be neglected, still leading to a smooth convergence to the maneuver aerodynamic coefficients. In coupled configurations, however, equating the coupling terms to zero resulted in slow convergence, with undesirable oscillations of the values of the trim variables. In any case, the derivative estimates can be quite crude, which might cause large overshoots of the correcting terms of Eq. (12). Relaxation can be used to avoid excessive overshoots.

The variation of the angle of attack is introduced to the CFD solver as a change in the far-field conditions and is therefore easy to implement. The control surface deflections require a change in the configuration and regeneration of the aerodynamic grid. This is done in the same manner as in the case of accounting for elastic deformations, by use of an elevator deflection mode with blended root

deflections to avoid geometric discontinuities in the aerodynamic grid. Angular rates associated with the maneuver are introduced by the addition of terms to the fluid dynamics equations to account for the fact that they are written in a rotating system.[19]

Structural Optimization

The aeroelastic CFD code was integrated with the ASTROS[1] code that has the ability to optimize the structure for minimum weight with simultaneous constraints from several disciplines and for multiple boundary conditions. To clarify the optimization scheme of this section, it is described in the way it was applied to the optimization case of the next section. The optimization model is the wing–fuselage–tail finite element model shown in Fig. 1.

Two types of constraints at two boundary conditions were considered: a constraint on the von Mises stresses in the wing elements at a symmetric 3-g pullup, and a constraint on aileron effectiveness at an antisymmetric roll. Both constraints require the evaluation of the aerodynamic loads, each at a different set of boundary conditions. Only the symmetric maneuver loads were computed in this study within the CFD code, whereas the aerodynamic loads in antisymmetric roll were computed by the USSAERO linear aerodynamic module of ASTROS. In general, the designer can choose either to perform every aerodynamic load evaluation by a separate CFD run (several CFD runs can be performed at the same time in parallel) or to limit the use of CFD only to design cases that would benefit the most from the more accurate evaluation of the aerodynamic loads.

The main difficulty in integrating the maneuver loads computations with a structural optimization analysis arises from the facts that the CFD analysis is computationally intensive and that repeated analyses are required during the structural optimization. Typical time measures for the CFD and finite element models of this study are 7 h for a CFD maneuver load analysis compared with 5 min for structural optimization. It is therefore impractical to perform a complete maneuver load analysis at every optimization step. Instead, several optimization runs are performed during the maneuver analysis, in which each optimization is performed with nonconverged maneuver loads. The combined maneuver–optimization run follows these steps:

1) The CFD maneuver run starts with a baseline structure and pauses several times during the steady-state flowfield convergence for structural optimization. These pauses are in addition to the pauses for elastic deformations and maneuver trim, which were discussed in the preceding section.

2) Each optimization pause starts with mapping the nonconverged maneuver loads to the structural grid by

$$\{\boldsymbol{F}_S\} = [T_{AS}]^T \{\boldsymbol{F}_A\} \tag{13}$$

where $[T_{AS}]$ is the transformation matrix from Eq. (4). This relation is derived from Eq. (4) and from the principle of virtual work.

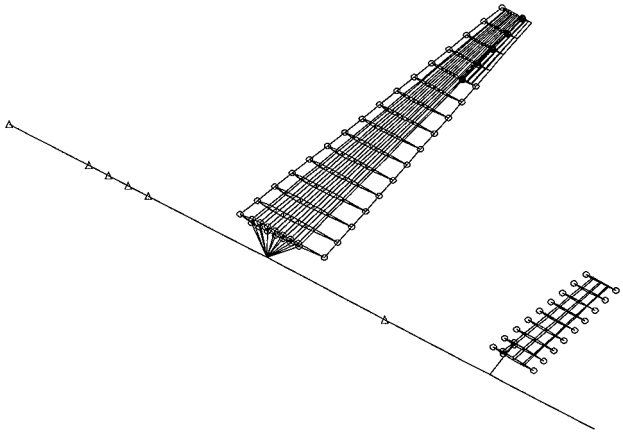

Fig. 1 Finite element model.

3) The loads are applied to the structure as a virtually fixed set of loads. These loads do not provide exactly the required maneuver aerodynamic coefficients both because they are extracted from a nonconverged maneuver analysis and because of the weight changes during the optimization. Application of the regular aeroelastic trim procedure in ASTROS would be incorrect because the loads already include aeroelastic effects. Therefore, at each optimization step, the aircraft is trimmed by use of the linear rigid derivatives of the aerodynamic coefficients. These trim corrections are not exact, but they are adequate for interim optimization runs and are reduced to zero as the entire maneuver optimization process converges.

4) The nonlinear maneuver case is joined by other nonlinear or linear loading cases and by design cases from other disciplines, such as aileron effectiveness and flutter, and structural optimization is performed.

5) A new modal database is created for the currently optimized structure at the final-analysis stage of the optimization. The new vibration modes and generalized stiffness matrices are used to update the modal database in the CFD run, which then resumes the regular aeroelastic CFD run.

With several optimization runs performed during the iterative process, there is no need to calculate the sensitivities of the nonlinear maneuver loads to design changes, which would create a major numerical difficulty.

Numerical Example

Aircraft Model

A simple transport aircraft model that has all the features necessary to verify the proposed methodology was created. The model aircraft includes a fuselage, wing, aileron, and all-movable tail. The wing and the elevator are similar in shape and structure—both are tapered and swept aft. The cross-section profiles of the wing and elevator are scaled NACA0012 symmetric profiles. Table 1 summarizes the wing and tail geometrical dimensions. The fuselage is 20 m long.

For the aerodynamic analysis, an H-type grid topology is used. Taking advantage of the multizone capability of the CFD code, the grid is divided into 24 zones, each describing a logical component such as wing upper/lower surface, fuselage, etc. Figure 2 describes i, k- and j, k-constant grid surfaces (only every other grid line is shown). The entire flowfield contains approximately 500,000 grid points.

A general view of the structural model is given in Fig. 1. It has approximately 1000 degrees of freedom. The torsion boxes of the wing and tail and the aileron are modeled in detail with elements representing skin, ribs, spars, spar caps, and stringers. Grid points are added along the leading and the trailing edges for an adequate surface spline. These points are rigidly connected to the front and the rear spars. The fuselage component is modeled as a flexible beam. Table 2 summarizes the weights of the half-aircraft model.

Table 1 Wing and tail geometrical dimensions

Parameter	Wing	Tail
Aspect ratio	10	6.4
Half span, m	10	4
Root chord, m	3	1.5
Leading-edge sweep angle, deg	20	20
Taper ratio	0.333	0.667

Table 2 Weight summary: half aircraft

Component	Weight, kg
Wing	384.6
Aileron	8.5
Elevator	98.5
Fuselage	
Structure	2700.0
Fuel	2000.0
Engine	700.0
Total weight	5891.6

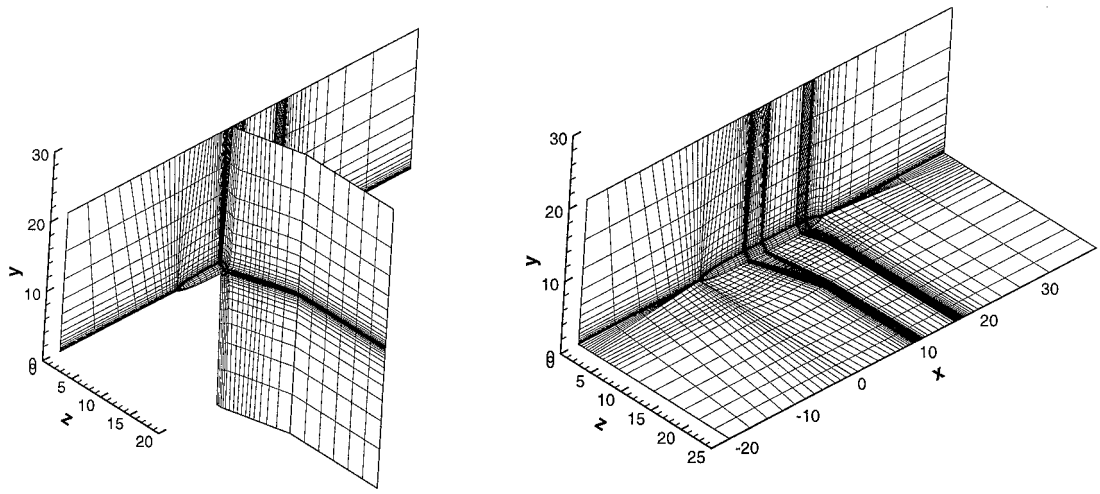

Fig. 2 Aerodynamic grid: *i*, *k*- and *j*, *k*-constant surfaces.

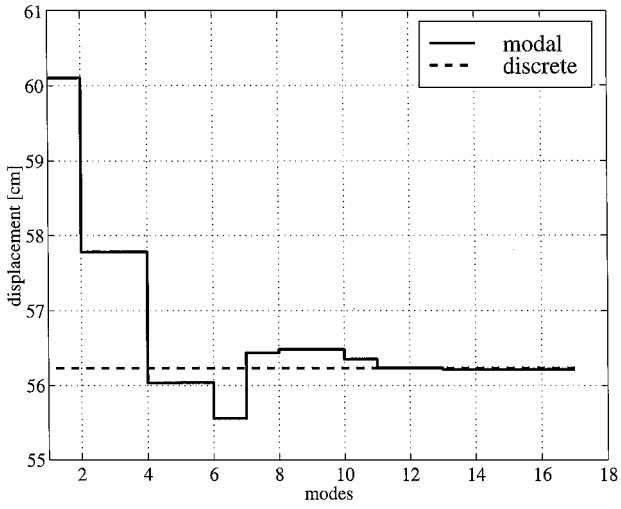

Fig. 3 Wing-tip leading-edge displacements based on modal coordinates.

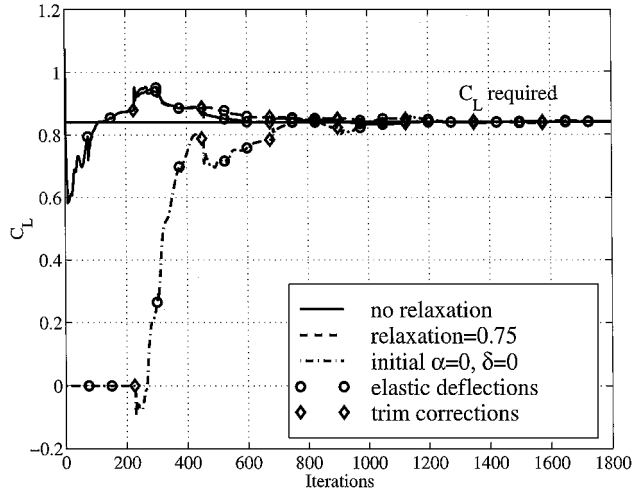

Fig. 4 C_L convergence history.

The wing weighs 384.6 kg, of which 284.6 kg is the weight of the torsion-box structure that is subjected to optimization. A modal analysis is performed to provide the 15 low-frequency vibration modes and the corresponding generalized stiffness matrix required for the CFD maneuver analysis.

Because the structural modes are used in the nonlinear aeroelastic analysis to describe elastic-shape deformations, a convergence study was performed to learn about the number of modes required for an adequate representation of the elastic deformations. The displacements at several points on the aircraft (such as the leading and the trailing edges of the wing and the elevator tip) were calculated in an aeroelastic analysis performed by ASTROS, using linear aerodynamics, with the model aircraft maneuvering at Mach number 0.85, an altitude of 11,000 m, and in an angle of attack of 5 deg with the elevator not rotated. The same analysis was performed with modal coordinates. Figure 3 presents the modal-based displacement of the wing-tip leading edge, as calculated with various number of modes, in comparison with the displacement calculated in the discrete approach (the dashed line). It is seen that the wing-tip leading-edge displacement converged to the discrete-coordinate solution with only the first 12 elastic modes taken into account. The same results were obtained for the other examined points. Consequently the nonlinear aeroelastic analysis was performed with 15 vibration modes, of which the first 2 are rigid-body modes and the remaining 13 are elastic.

Maneuver Analysis

As mentioned in the preceding section, only the symmetric maneuver loads were computed with a CFD run, whereas the antisymmetric loads were computed in ASTROS with linear aerodynamics. The following description is of a 3-g pullup maneuver of the baseline structure at Mach 0.85 and a height of 11,000 m, which defines a pitch rate of $\dot{\theta} = (n - 1)g/V = 0.066$ rad/s and corresponds to required lift and moment coefficients of $C_L = 0.84$ and $C_M = 0$, respectively. Maneuver load computations performed with the same aerodynamic model and a similar structural model are described in Ref. 18. The new maneuver–loads results shown below demonstrate the process robustness and form the basis for subsequent application in structural optimization.

The CFD run starts with a computational grid that describes the undeformed aircraft jig shape and with an initial guess of the trim parameters, which are the angle of attack and the elevator deflection. In the shown run cases the CFD convergence process was paused after every 75 iterations for either elastic or trim corrections, in which the first two in every three corrections were elastic and the third one was a trim correction. These steps were repeated until the flowfield converged and the required maneuver coefficients were obtained.

Figures 4 and 5 show the history of convergence of the lift and the moment coefficients, respectively, indicating the approach to their required values. Plots are shown for three different run cases. The solid curve describes a run case that was started with the trim parameters that were obtained from a reference linear maneuver analysis

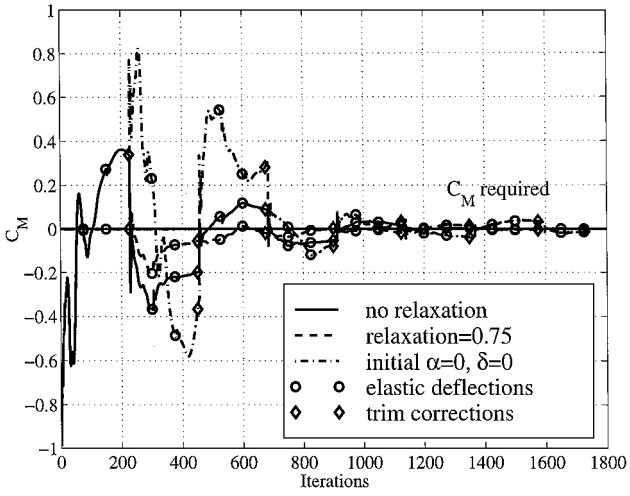

Fig. 5 C_M convergence history.

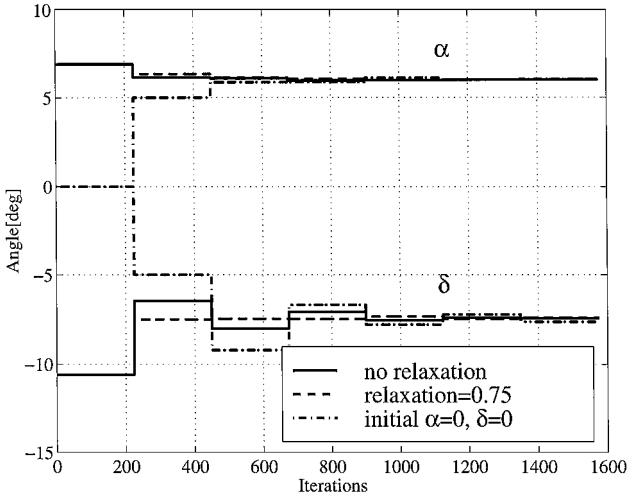

Fig. 6 α and δ convergence history.

with ASTROS: $\alpha = 6.9$ deg and $\delta = -10.6$ deg, with the trim corrections of Eq. (12) performed with the linear aerodynamic derivatives. The dashed curve describes a run case in which relaxation factor of 0.75 was used, meaning that the trim corrections were only 75% of those calculated with the linear aerodynamic derivatives. The dashed–dotted curve describes a run case that was initialized with zero angle of attack and control surface deflection and performed with no relaxation. This extreme case is presented to demonstrate the robustness of the maneuver analysis with respect to the initial guess of trim parameters. It is seen that only few elastic and trim updates are required for convergence. All three runs ended with practically the same values of trim parameters. The convergence was more rapid when the process was started with a good guess of the trim parameters and slightly more rapid when a relaxation of trim corrections was applied. Figure 6 shows the values of the angle of attack and elevator deflection angle throughout the CFD iterations. The fact that all three runs converged smoothly indicates the scheme robustness with respect to the initial guess of trim parameters and with respect to the derivatives of the aerodynamic coefficients that are used for trimming the aircraft.

A wing section at 82% of the span and the pressure field around it are shown in Fig. 7, in which a shock wave at about 85% of the chord can be observed. Figure 8 presents the differential pressure coefficient (ΔC_p) distribution along this wing section, comparing the linear and nonlinear values. It is notable that the nonlinear and the linear pressure distributions significantly differ from one another. The nonlinear chordwise center of pressure is moved aft compared with the linear one, causing a nosedown moment and an increased section washout angle. The difference between the computed linear and nonlinear ΔC_p distributions is attributed to the different aerodynamic theories. For comparison, results of another maneuver analysis, performed at low Mach number (1-g level flight at Mach 0.5 at a height of 5000 m) are presented in Fig. 9. The linear ΔC_p is presented for the trimmed maneuver and for a nontrimmed case for which the airloads were evaluated at the nonlinear trim angle of attack and elevator deflection angle. It can be seen that at low Mach numbers the linear and nonlinear ΔC_p distributions are very close, as predicted by aerodynamic theories.

Table 3 compares the maneuver trim results obtained with the CFD run with those of ASTROS for the baseline and for the optimized structures. It can be observed that there are significant differences in the trimmed elevator deflection angles that are due to

Table 3 Maneuver trim results

	Baseline		Optimized	
Parameter	ASTROS	CFD	ASTROS	CFD
Angle of attack, deg	6.9	6.0	7.1	6.1
Elevator deflection, deg	−10.6	−7.4	−9.8	−7.2
Wing-tip leading-edge deflection, m	0.79	0.82	1.08	1.21
Wing-tip washout angle, deg	0.8	2.4	1.3	3.9

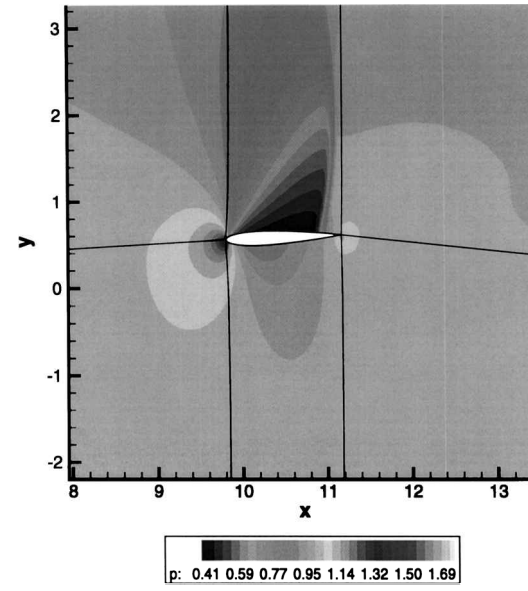

Fig. 7 Pressure field around wing section at 82% of the span.

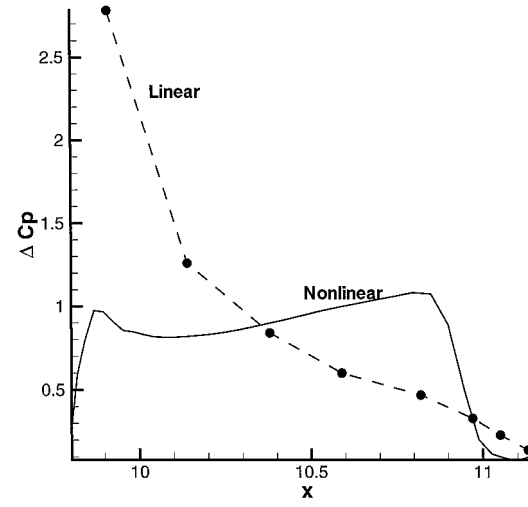

Fig. 8 Differential pressure coefficient distribution at 82% of the span.

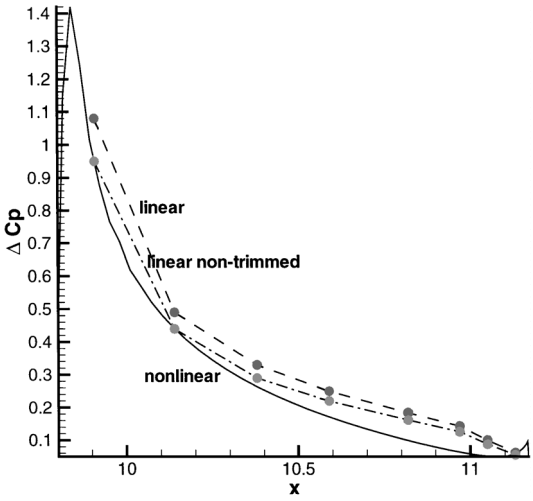

Fig. 9 Differential pressure coefficient distribution at Mach 0.5.

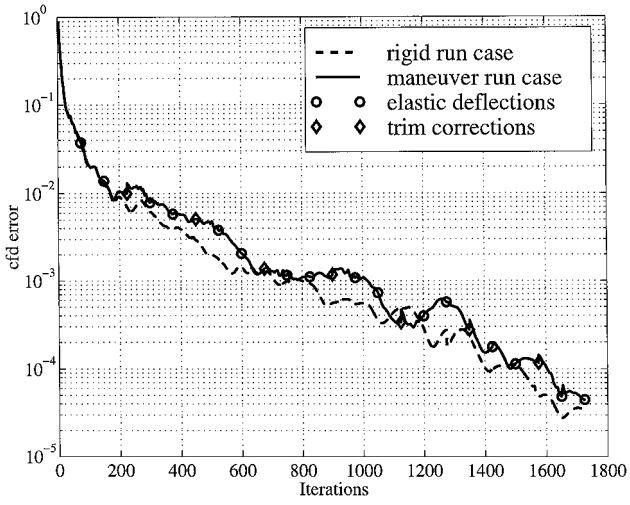

Fig. 10 Residual decay history.

the different aerodynamic moments, and differences in the deformed shape of the maneuvering aircraft. Such differences can significantly affect the structural design, as shown below.

A measure of convergence of the CFD solution is the reduction of the residual, defined by the average error in the flow equations. Figure 10 shows the history of residual decay of the elastic maneuver case compared with that of the rigid one. It is seen that the disturbances to the flowfield caused by the shape updates and trim corrections have little effect on the residual, and that the total number of iterations required for flowfield convergence is almost the same for the maneuver and the rigid run cases. The extra CPU time required for grid update, following every elastic deformation or trim correction, was approximately 2 s, compared with approximately 60 s required for each CFD iteration. Therefore, because only a few elastic and trim corrections are made, the total extra CPU time required for the inclusion of elastic and trim effects in a typical flow computation is negligible.

Design Variables and Constraints

The wing torsion box is divided into five spanwise segments. At each segment, the design variables control the thicknesses of the wing skins, the ribs, the front and the rear spar webs, and the cross-section area of the front and the rear spar caps and the stringers, resulting in a total of 35 design variables. The torsion box is optimized for minimum weight under the following constraints:

1) The von Mises stresses are constrained by two-thirds of the material ultimate stress (280 MPa) in a symmetric 3-g pullup maneuver at Mach 0.85, $h = 11{,}000$ m.

2) The aileron effectiveness, defined by the ratio of rolling moment coefficients due to aileron deflection and due to roll rate, $C_{l_{\delta a}}/C_{l_{\bar{p}}}$, is constrained by AE ≥ 0.14 in an antisymmetric roll maneuver at Mach 0.85, $h = 11{,}000$ m.

Structural Optimization

The combined loads–optimization process was executed by the replacement of every third trim correction in a maneuver load run with a structural optimization run. The optimization runs were performed with the standard discrete-coordinate static-aeroelastic module of ASTROS, modified to accommodate the CFD loads as a fixed set of loads to which a trim correction is added in every optimization step, as discussed in the preceding section. Each ASTROS optimization step required ~60 s. With larger structural models, the modal-based optimization method[22,23] can be used to keep the cost of the structural optimization relatively low.

To evaluate the effects of nonlinear aerodynamics on the structural design, the same optimization run case was performed by the standard ASTROS, with both design cases based on linear aerodynamics. The maneuver trim parameters and the elastic wing-tip deformations of the optimized structure are shown in Table 3, comparing the CFD-based optimization with the standard ASTROS optimization. The largest difference in aeroelastic behavior between the CFD and the linear cases is in the wing-tip washout that is three times larger in the CFD cases. The effects on the structural design are discussed below. Figures 11 and 12 show the history of convergence of the lift and the moment coefficients, in which it is seen that the required C_L is slightly reduced from 0.84 to 0.83 on

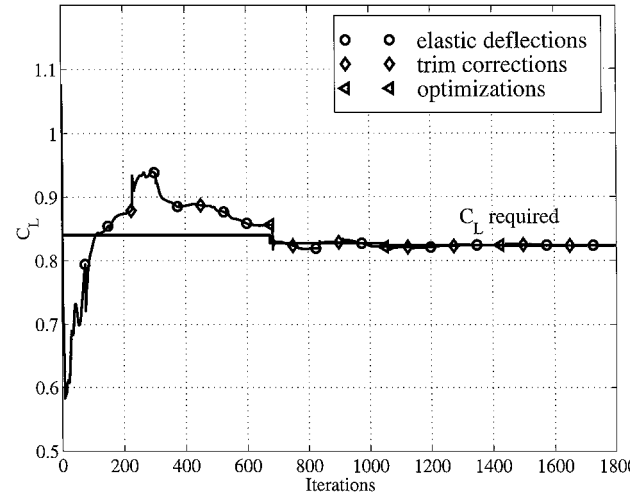

Fig. 11 C_L convergence history: optimization case.

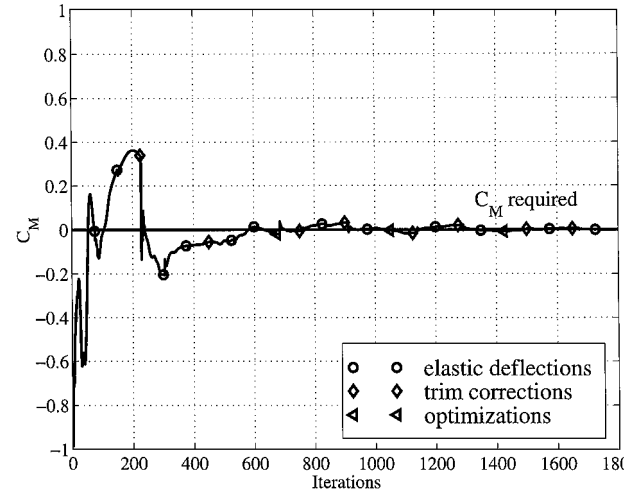

Fig. 12 C_M convergence history: optimization case.

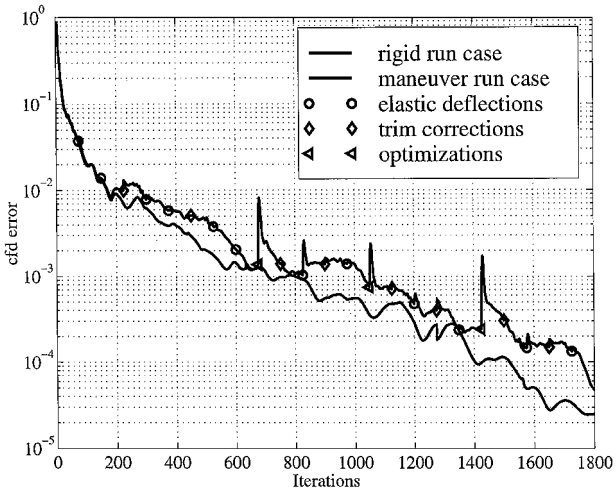

Fig. 13 Residual decay history: optimization case.

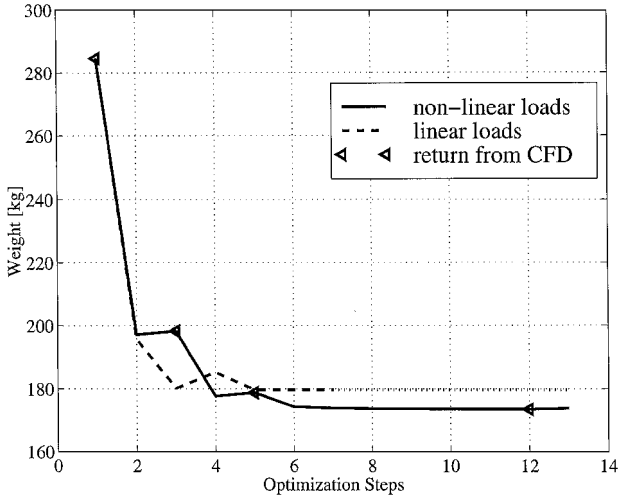

Fig. 14 Wing structure weight history.

return from the first structural optimization because of weight reduction. Figure 13 shows the history of residual decay of the combined maneuver–optimization run case. On return from the optimization, when the airloads are applied to the optimized structure that is less stiff, new deformations are obtained. It can be seen that the shape change increases the CFD error, which then rapidly decays. The total number of iterations required for convergence of the combined loads–optimization run is almost the same as that for a CFD run with a fixed shape.

The structural optimization in ASTROS is performed by several gradient-based design steps, with each step based on a single-variable optimization. The reference optimization performed by ASTROS with linear aerodynamics converged in seven optimization steps, after which the variable-structure weight was reduced from 284.6 to 180.0 kg. The same design task with the nonlinear maneuver loads led to a variable-structure weight of 173.9 kg. Figure 14 shows the history of weight reduction during the optimization, comparing the reference ASTROS optimization with the CFD-based optimization. The 4% difference between the optimal weight of the two wing designs is not small, considering the facts that both load distributions yield the same design maneuvers and that the optimization was controlled not only by the maneuver stresses, but also by the demand for aileron effectiveness, which was similarly analyzed in both design cases by linear aerodynamics. A distinct effect of the nonlinear loads can be observed when the optimal values of the design variables of the two designs are examined (Fig. 15). Although the skins converged to almost the same values at the two designs, with small differences near the tip that were due to the different washouts, significant differences were found in the front and the rear spars. Material is moved in the CFD-based optimization from the front spar to the rear spar because the centers of chordwise pressure distributions are significantly aft of those of linear aerodynamics, which also cause the larger wing-tip washout.

Conclusions

This paper presented efficient methodology for performing structural optimization with static-aeroelastic considerations, in which the aerodynamic loads are provided by a nonlinear CFD scheme. The maneuver analysis exhibited good convergence properties, with the number of iterations required for convergence almost the same

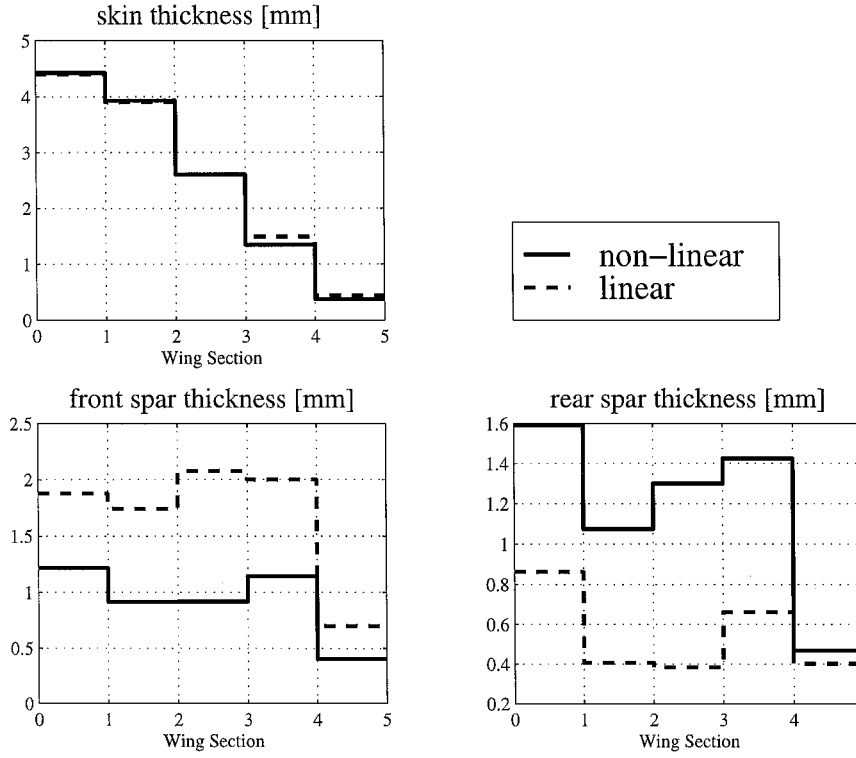

Fig. 15 Optimal design variables.

as that of a regular CFD analysis for a fixed shape. The scheme was found to be robust with respect to initial guess of the trim variables and of the derivatives of the aerodynamic coefficients that were used for trimming the aircraft. The use of the modal approach for representing the structure provided an accurate, simple, and efficient way of interfacing the CFD and the structural models, calculating elastic deformations, and applying them to the CFD grid. The formulation of the elastic-shape deformations was done in a manner that allows preserving either the jig shape or the nominal cruise shape throughout the optimization. A numerical example of a maneuvering free aircraft demonstrated significant differences in trim variables and elastic deformations between linear and nonlinear aerodynamic cases, especially in the wing-tip washout. The combined maneuver–optimization analysis showed very good simultaneous convergence of both the aerodynamic loads and the structural design, with the number of CFD iteration similar to those required for maneuver analysis only. The extra CPU time required for the elastic deformations and trim corrections and the time required for structural optimization were negligible compared with the CFD run time. Comparison between linear and CFD-based designs showed significant differences in both total weight and local structural gauge distribution. The study established a framework for integrated aircraft optimization in which some disciplines are based on nonlinear numerical schemes and others on linear methods. The framework allows several CFD-based maneuver cases to be included simultaneously by means of parallel computation.

References

[1]Neill, D. J., Johnson, E. H., and Canfield, R. A., "ASTROS—A Multidisciplinary Automated Structural Design Tool," *Journal of Aircraft*, Vol. 27, No. 12, 1990, pp. 1021–1027.

[2]Moore, G. J., "MSC/NASTRAN Version 68 Design Sensitivity and Optimization User's Guide," MacNeal-Schwendler Corp., Los Angeles, 1994.

[3]Woodward, F. A., "An Improved Method for the Aerodynamic Analysis of Wing-Body-Tail Configuration in Subsonic and Supersonic Flow, Part I—Theory and Applications," NASA CR-2228, May 1973.

[4]Albano, E., and Rodden, W. P., "A Doublet-Lattice Method for Calculating Lift Distributions on Oscillating Surfaces in Subsonic Flows," *AIAA Journal*, Vol. 7, No. 2, 1969, pp. 279–285.

[5]Whitlow, W., Jr., and Bennett, R. M., "Application of a Transonic Potential Flow Code to the Static Aeroelastic Analysis of Three-Dimensional Wings," *Proceedings of the 23rd Structures, Structural Dynamics, and Materials Conference*, Vol. 2, AIAA, New York, 1982, pp. 267–276.

[6]Agrell, N., and Hedman, S. G., "Calculations of Transonic Steady State Aeroelastic Effects for Canard Airplane," *Proceedings of the 13th Congress of the International Council of the Aeronautical Sciences, AIAA Aircraft System and Technology Conference*, ICAS-82-2.1.2, International Council of the Aeronautical Sciences, Seattle, WA, 1982, pp. 59–66.

[7]Pittman, J. L., and Giles, G. L., "Combined Nonlinear Aerodynamic and Structural Method for the Aeroelastic Design of a Three-Dimensional Wing in Supersonic Flow," *Proceedings of the Applied Aerodynamics Conference*, AIAA, New York, 1986, pp. 36–44.

[8]Tatum, K. E., and Giles, G. L., "Integrating Nonlinear Aerodynamic and Structural Analysis for a Complete Fighter Configuration," *Journal of Aircraft*, Vol. 25, No. 12, 1988, pp. 1150–1156.

[9]Vinh, L., Edwards, J. W., Seidel, D. A., and Batina, J. T., "Transonic Stability and Control of Aircraft Using CFD Methods," *Proceedings of the AIAA Atmospheric Flight Mechanics Conference*, AIAA, Washington, DC, 1988, pp. 394–404.

[10]Batina, J. T., Seidel, D. A., Bland, S. R., and Bennet, R. M., "Unsteady Transonic Flow Calculations for Realistic Aircraft Configurations," *Journal of Aircraft*, Vol. 26, No. 1, 1989, pp. 21–28.

[11]Schuster, D. M., Vadyak, J., and Atta, E., "Static Aeroelastic Analysis of Fighter Aircraft Using a Three-Dimensional Navier–Stokes Algorithm," *Journal of Aircraft*, Vol. 27, No. 5, 1900, pp. 820–825.

[12]Schuster, D. M., "An Application of a Navier–Stokes Aeroelastic Method to Improve Fighter Wing Performance at Maneuver Flight Conditions," *Journal of Aircraft*, Vol. 32, No. 1, 1995, pp. 77–83.

[13]Guruswamy, G. P., "Coupled Finite-Difference/Finite-Element Approach for Wing-Body Aeroelasticity," *Proceedings of the 4th Symposium on Multidisciplinary Analysis and Optimization*, AIAA, Washington, DC, 1992, pp. 1–12.

[14]Obayashi, S., and Guruswamy, G. P., "Convergence Acceleration of Navier–Stokes Solver for Efficient Static Aeroelastic Computations," *AIAA Journal*, Vol. 33, No. 6, 1995, pp. 1134–1141.

[15]Karpel, M., Yaniv, S., and Livshits, D. S., "Integrated Solution for Computational Static Aeroelastic Problems," *Proceedings of the 6th Symposium on Multidisciplinary Analysis and Optimization*, AIAA, Reston, VA, 1996, pp. 262–272.

[16]Sheena, Z., and Karpel, M., "Static Aeroelastic Analysis Using Aircraft Vibration Modes," *Proceedings of the 2nd International Symposium on Aeroelasticity and Structural Dynamics*, DGLR, Bonn, Germany, 1985, pp. 229–232.

[17]Karpel, M., and Sheena, Z., "Structural Optimization for Aeroelastic Control Effectiveness," *Journal of Aircraft*, Vol. 26, No. 8, 1989, pp. 493–495.

[18]Raveh, D. E., Karpel, M., and Yaniv, S., "Non-Linear Design Loads for Maneuvering Elastic Aircraft," *Proceedings of the 38th Israel Annual Conference on Aeroepace Sciences*, Technion—Israel Inst. of Technology, Haifa, Israel, 1998, pp. 150–160.

[19]Yaniv, S., "Navier–Stokes Calculations for Rotating Configurations: Implementation for Rockets," *Journal of Spacecraft*, Vol. 33, No. 5, 1996, pp. 756–758.

[20]Harder, R. L., and Desmarais, R. N., "Interpolation Using Surface Splines," *Journal of Aircraft*, Vol. 9, No. 2, 1972, pp. 189–191.

[21]Rodden, W. P., and Johnson, E. H., "MSC/NASTRAN Version 68 Aeroelastic Analysis User's Guide," MacNeal-Schwendler Corp., Los Angeles, 1994.

[22]Karpel, M., Moulin, B., and Love, M. H., "Modal-Based Structural Optimization with Static Aeroelastic and Stress Constraints," *Journal of Aircraft*, Vol. 34, No. 3, 1997, pp. 433–440.

[23]Karpel, M., "Modal-Based Enhancement of Integrated Structural Design Optimization Schemes," *Journal of Aircraft*, Vol. 35, No. 3, 1998, pp. 437–444.